ARTICLE

Tailorable Electrocatalytic 5-Hydroxymethylfurfural Oxidation and H$_2$ Production: Architecture−Performance Relationship in Bifunctional Multilayer Electrodes

Minju Park,[||] Minsu Gu,[||] and Byeong-Su Kim*

Read Online

ACCESS | Metrics & More | Article Recommendations | SI Supporting Information

ABSTRACT: Water electrocatalytic splitting is considered as an ideal process for generating H$_2$ without byproducts. However, in the water-splitting reaction, a high overpotential is needed to overcome the high-energy barrier due to the slow kinetics of the oxygen evolution reaction (OER). In this study, we selected the 5-hydroxymethylfurfural (HMF) oxidation reaction, which is thermodynamically favored, to replace the OER in the water-splitting process. We fabricated three-dimensional hybrid electrocatalytic electrodes *via* layer-by-layer (LbL) assembly for simultaneous HMF conversion and hydrogen evolution reaction (HER) to investigate the effect of the nanoarchitecture of the electrode on the electrocatalytic activity. Nanosized graphene oxide was used as a negatively charged building block for LbL assembly to immobilize the two electroactive components: positively charged Au and Pd nanoparticles (NPs). The internal architecture of the LbL-assembled multilayer electrodes could be precisely controlled and their electrocatalytic performance could be modified by changing the nanoarchitecture of the electrode, including the thickness and position of the metal NPs. Even with a composition of the identical constituent NPs, the electrodes exhibited highly tunable electrocatalytic performance depending on the reaction kinetics as well as a diffusion-controlled process due to the sequential HMF oxidation and the HER. Furthermore, a bifunctional two-electrode electrolyzer for both the anodic HMF oxidation and the cathodic HER, which had an optimized LbL-assembled electrode for each reaction, exhibited the best full-cell electrocatalytic activity.

KEYWORDS: electrocatalyst, 5-hydroxymethylfurfural, hydrogen evolution reaction, biomass reforming, layer-by-layer assembly, nanoarchitectures
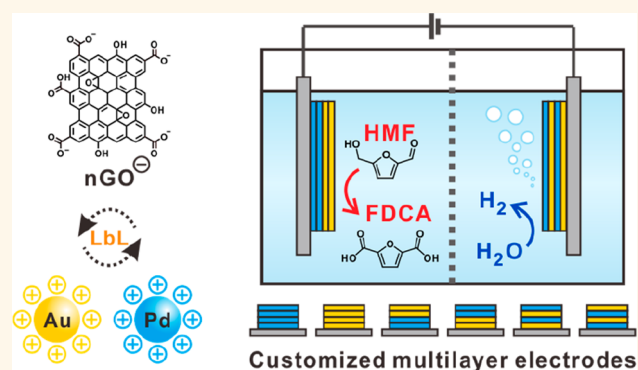
The critical concerns regarding the global energy demand and climate-change issues have motivated considerable efforts for developing alternative energy.[1,2] As an ecofriendly energy carrier, H$_2$ is anticipated to play a significant role in future sustainable energy. However, most H$_2$ is conventionally produced through the Ni-catalyzed conversion of CH$_4$ to H$_2$, which inevitably produces greenhouse gases, such as CO and CO$_2$.[3] Therefore, water splitting is considered as an ideal process to generate H$_2$ without byproducts.[4,5] However, in the water-splitting reaction, a high overpotential is needed to overcome the high-energy barrier. Generally, the overall reaction kinetics are limited by

the anodic oxygen evolution reaction (OER) because of the sluggish four-electron transfer reaction in water oxidation in comparison with the cathodic hydrogen evolution reaction (HER). The OER requires an applied voltage of at least 1.23 V to provide the thermodynamic driving force. Because of the

Scheme 1. LbL-Assembled Hybrid 3D Multilayer Thin-Film Electrodes for Bifunctional HMF Oxidation and H$_2$ Production
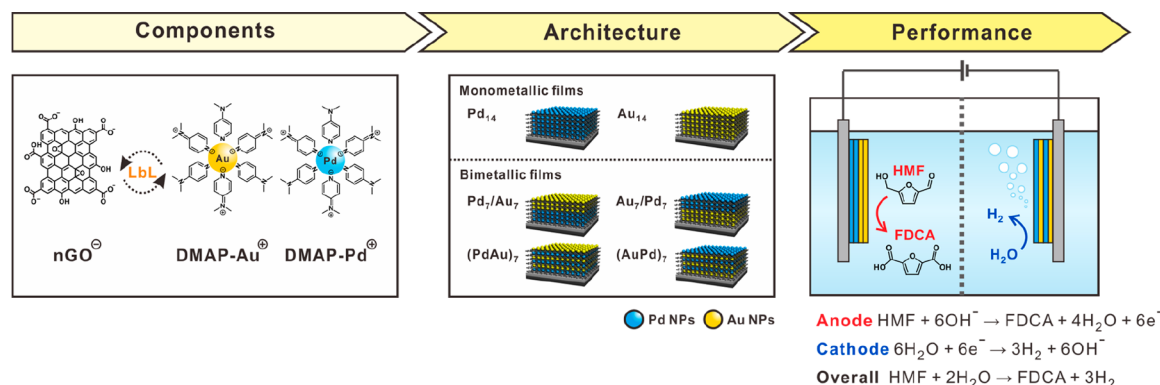
practical overpotentials associated with the reaction kinetics, a substantially higher operating voltage, typically in the range of 1.8−2.0 V, is generally required.[6,7] Thus, the production cost is not competitive with the commercial production from natural gas, owing to the high overpotential encountered in water electrolysis. Furthermore, the coexistence of H$_2$ and O$_2$ gases, which may lead to the formation of an explosive H$_2$/O$_2$ mixture, requires additional gas-separation systems.[8]

Recent efforts have been directed toward replacing the anodic OER with reactions involving more easily oxidizable molecules, such as methanol, ethanol, ammonia, and urea, which is referred to as electrochemical reforming.[9−13] There are several requirements for replacing the OER in a water-splitting reaction. First, the kinetics should be faster than those of the OER, with more favorable energetics when coupled to the HER. Second, the product of the replaced reaction should yield a higher chemical value than O$_2$. Third, the reacting substrate must exhibit a high solubility in an aqueous solution for enabling concurrent H$_2$ production.

Because these requirements highlight the need for a new substrate, we selected the 5-hydroxymethylfurfural (HMF) oxidation reaction to replace the OER in this study. HMF has been classified as a top biomass-derived building block chemical for producing valuable products; for example, 2,5-furandicarboxylic acid (FDCA)—one of the products of HMF oxidation—is as an important monomer for synthesizing the renewable polymer poly(ethylene furanoate) in place of petroleum-derived poly(ethylene terephthalate).[1,14,15] Although there are several ways to selectively oxidize HMF to FDCA through organic chemical reactions, they often require a harsh reaction environment, for example, a high temperature (>100 °C) and high-pressure O$_2$ (0.3−2.4 MPa).[16−19] Therefore, it is highly desirable to develop efficient methods that use mild conditions and novel catalysts to produce FDCA.

Electrocatalytic HMF oxidation has attracted attention as a promising sustainable strategy because it can be performed under ambient conditions without toxic chemicals.[19−21] For example, Li *et al.* employed Au/Pd alloy nanoparticles (NPs) to oxidize HMF to FDCA.[22] The Au/Pd alloy NPs exhibited better electrocatalytic performance than individual NPs for producing FDCA. In a more recent study, Sun and co-workers integrated HMF oxidation and H$_2$ generation from water splitting with the excellent catalytic performance of Ni-based catalysts.[23−26] Although outstanding activity was achieved, these studies only focused on developing new materials to enhance the electrocatalytic performance; thus far, the

structure of the electrode has not been a subject of intensive investigation. For further advancing the outstanding individual material properties in a platform of the electrode assembled, it is highly desirable to deduce the architecture−performance relationships in the electrode. Moreover, an in-depth mechanistic analysis can further shed a light on the design of functional electrodes with optimal performance.

In this regard, we propose the fabrication of a tailorable three-dimensional (3D) hybrid multilayer electrode *via* layer-by-layer (LbL) assembly for simultaneous HMF conversion and H$_2$ production. We investigate the relationships between the electrocatalytic activity and the nanoarchitectures of bimetallic electrodes by controlling the sequence of metal NPs (Scheme 1).

As one of the most versatile fabrication methods for fabricating highly ordered multilayer architectures, LbL assembly has the unique capability to produce diverse materials with nanoscale control of both the structure and composition. Specifically, nanosized graphene oxide (nGO) is used as a negatively charged building block for LbL assembly to immobilize two electroactive components, such as positively charged Au and Pd NPs. We highlight how the internal architecture of LbL-assembled multilayer electrodes, not only the film thickness (*i.e.*, the amount of NPs) but also the position of each metal NP within 3D multilayer thin-film electrodes, can be precisely controlled, in addition to how it affects the electrode electrocatalytic performance in conjunction with the multiple reaction pathways of HMF oxidation. Even with the identical composition of constituent NPs, the electrodes exhibit highly tunable electrocatalytic performance depending on the reaction kinetics as well as the diffusion-controlled process involved in the sequential oxidation reaction of HMF. Furthermore, the bifunctional two-electrode electrolyzer coupled for both anodic HMF oxidation and the cathodic HER, which was independently optimized for each half-reaction, exhibits outstanding electrocatalytic activity in water-splitting electrolysis. We anticipate that the proposed concept can be employed to combine HER with many other organic reactions for establishing a valuable electrochemical reforming system.

RESULTS AND DISCUSSION

Design and Fabrication of Multilayer Electrodes. Initially, highly stable aqueous suspensions of nGO and metal NPs were synthesized to fabricate 3D LbL-assembled electrocatalytic electrodes *via* electrostatic interactions. In accordance with our previous study on diffusion-controlled
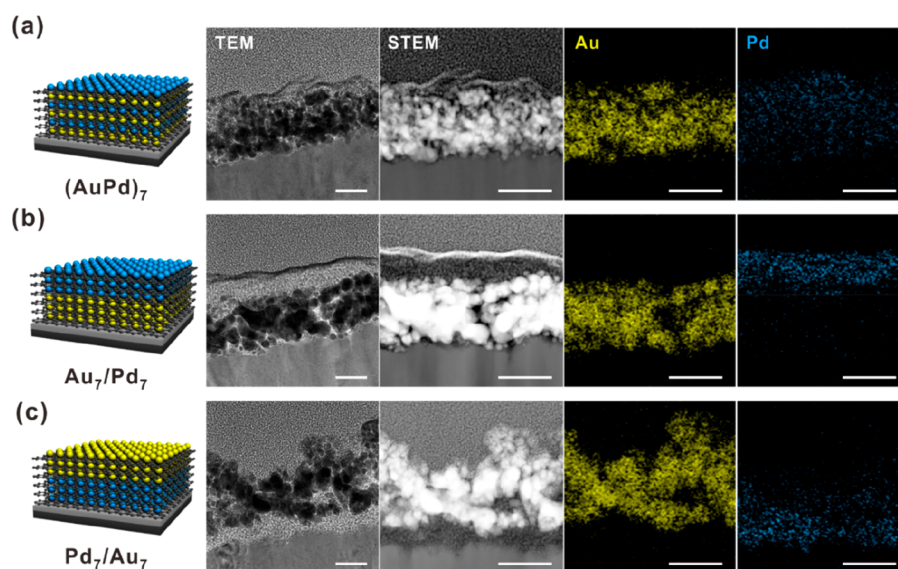
Figure 1. Architecture-controlled multilayer thin-film electrodes. Representative cross-sectional TEM, scanning TEM (STEM), and EDS mapping images of (a) $(AuPd)_7$, (b) Au_7/Pd_7, and (c) Pd_7/Au_7 multilayer thin-film electrodes assembled on an ITO-coated substrate (scale bar: 50 nm).

multilayer electrodes employing nGO, we prepared a negatively charged nGO suspension *via* exfoliation from a graphite nanofiber precursor.[27] In parallel, positively charged Au and Pd NP suspensions were prepared *via* the spontaneous phase transfer of an organic solvent into an aqueous phase using 4-(dimethylamino)pyridine (DMAP), to exclude the effect of electrochemical charge-transfer kinetics caused by using different capping layers on the surface of the metal NPs. The average diameters of the Au and Pd NPs were determined to be 5.8 and 3.4 nm, respectively, by transmission electron microscopy (TEM, Figure S1 in the Supporting Information).

Using these stable suspensions of positively charged Au and Pd NPs as electroactive species and the negatively charged nGO suspension as a catalytic support, we fabricated monometallic electrodes *via* LbL assembly onto indium tin oxide (ITO) substrates consisting of nGO and either Au or Pd NPs to obtain a thin-film electrode of $(nGO^-/Au^+)_n$ or $(nGO^-/Pd^+)_n$ (n = number of bilayers (BLs)). Furthermore, bimetallic hybrid electrodes composed of both Au and Pd NPs were assembled with various structures, including substrate/ $(nGO^-/Au^+)_n/(nGO^-/Pd^+)_n$, substrate/$(nGO^-/Pd^+)_n/$ $(nGO^-/Au^+)_n$, and substrate/$(nGO^-/Au^+/nGO^-/Pd^+)_m$ (m = number of tetralayers (TLs)). Hereafter, for simplicity, the monometallic thin-film electrodes are denoted as Au_n and Pd_n, and the bimetallic thin-film electrodes are denoted as Au_n/Pd_n, Pd_n/Au_n, and $(AuPd)_n$.

The successful linear growth of each multilayer electrode was monitored by the gradual increase of absorbance upon increasing the number of layers in UV−vis spectra (Figure S2a−d). The thickness of each multilayer film also exhibited a linear growth with an average BL thickness of 6.7 and 11.3 nm for a single BL of the Au_n and Pd_n multilayers, respectively, and 14.2 nm for a single TL of the $(AuPd)_n$ electrode (Figure S2e). To monitor the sequential adsorption behavior of the components, such as nGO, Au NPs, and Pd NPs, in the $(AuPd)_n$ multilayer electrodes, a quartz-crystal microbalance (QCM) was used to perform measurements with respect to the number of deposition steps (Figure S 2f). The average mass of each layer within a single TL was determined to be 0.21 μg

cm^{-2}, 6.35 μg cm^{-2}, and 1.03 μg cm^{-2} for nGO, Au NPs, and Pd NPs, respectively.

Using seven BLs of each metal NP electrode as a representative example, which exhibited the optimal electrocatalytic activity, the internal architecture of the multilayer film electrodes was controlled with various structures, such as a fully alternating $(AuPd)_7$ electrode and opposite structures of Au_7/Pd_7 and Pd_7/Au_7 multilayer electrodes. The nanoarchitectures of the fabricated thin-film electrode were examined *via* cross-sectional TEM (Figure 1) and atomic force microscopy (AFM) (Figure S3). The multilayer electrodes with different architectures were clearly observed with the aid of the contrast difference in elemental mapping between the Au and Pd NPs (Figure 1). According to the AFM images for the surface analysis, the root-mean-squared surface roughness (R_{rms}) values (averaged over $25 \times 25\ \mu m^2$) for the Pd_7/Au_7, Au_7/Pd_7, and $(AuPd)_7$ multilayer film electrodes were determined to be 85.8 ± 3.6, 55.1 ± 2.2, and 46.9 ± 7.0 nm, respectively. This tendency is in accordance with a previous study where large Au NPs were deposited on a surface, yielding a surface roughness significantly higher than that for smaller Pd NPs.[28]

Electrocatalytic Performance. Initially, we investigated the electrocatalytic oxidation of HMF for each electrode to identify the architecture−performance relationships for the electrocatalytic reaction. Because the OER was the major reaction competing with HMF oxidation, water oxidation in the absence of HMF was first investigated using one of the bimetallic Pd_7/Au_7 electrodes, which had the optimal performance for HMF oxidation (Figure S4). Without HMF, the linear sweep voltammetry (LSV) curve showed an anodic current onset at 1.53 V (*vs* reversible hydrogen electrode (RHE)), resulting from the OER. In contrast, the anodic onset potential was approximately 0.34 V (*vs* RHE) in the presence of 10 mM HMF, indicating that the oxidation of HMF was significantly favored over water oxidation.

To evaluate the electrocatalytic activity with respect to the thickness of the electrodes, we measured the LSV curves according to the number of BLs for Pd_n and Au_n electrodes
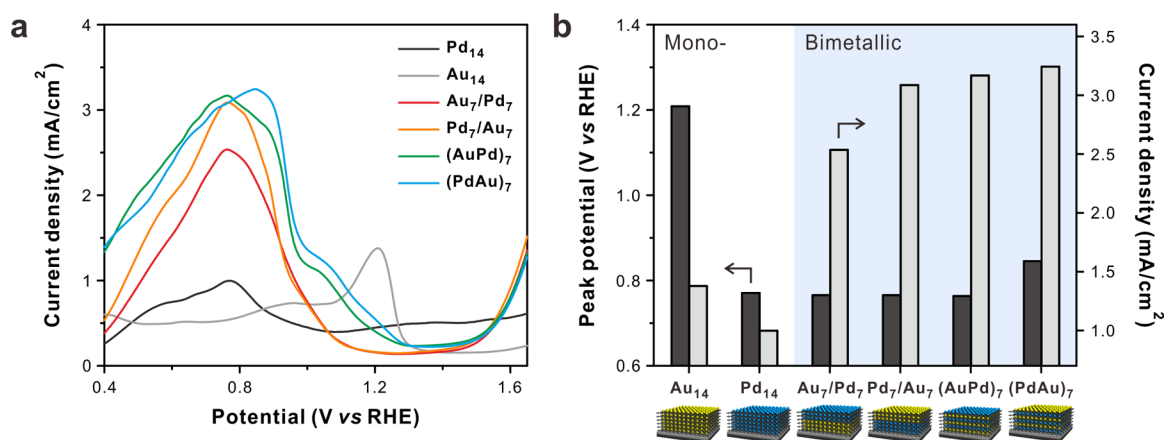
Figure 2. Electrocatalytic activity for the HMF oxidation reaction of all multilayer electrodes prepared in the study. (a) LSVs measured at a scan rate of 2.0 mV s^{-1} with 10 mM HMF in a 1.0 M KOH electrolyte and (b) comparison of the peak potential (black) and current density at the peak potential (gray) for each film electrode with the corresponding architecture.
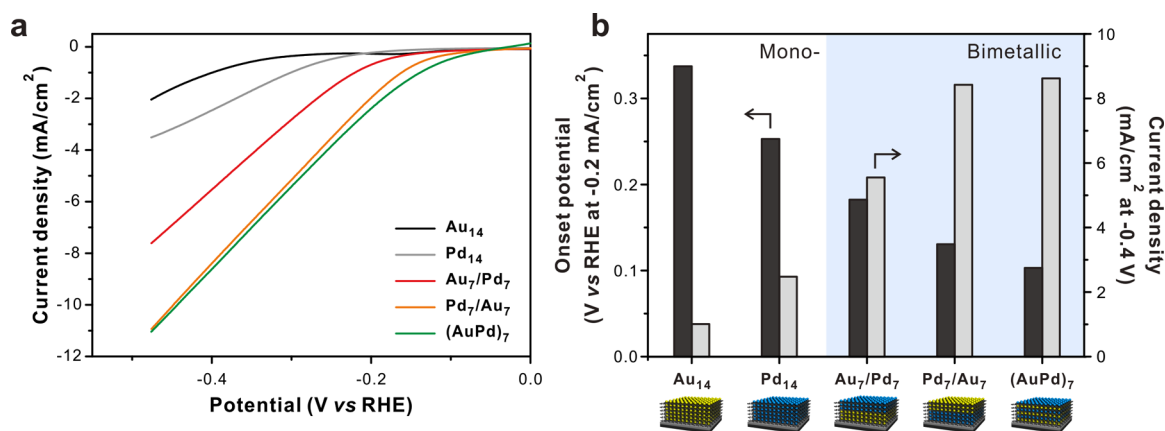

Figure 3. Electrocatalytic activity of multilayer electrodes for the HER. (a) LSVs of all electrodes prepared in the study, obtained at a scan rate of 2.0 mV s^{-1} with 10 mM HMF in a 1.0 M KOH electrolyte. (b) Comparison of the onset potential at -0.2 mA cm^{-2} (black bar) and the current density at -0.4 V (vs RHE) (gray bar) for each electrode.

(Figure S5a,b). In our previous studies, the performance of LbL-assembled multilayer electrodes was highly dependent on the number of layers (i.e., thickness), which is related to the concentration of electrocatalytically active NPs.[28−31] In LbL-assembled thin-film electrodes, the electrocatalytic performance is considerably influenced by their electrochemical kinetics and charge-transfer resistance (R_{ct}) owing to a facile mass transfer. Electrochemical impedance spectroscopy (EIS) was employed to evaluate the electrochemical kinetics and interfacial resistance of Au$_n$ and Pd$_n$ film electrodes ($n = 2-8$) (Figure S6 and Table S1). In the case of Au$_n$ films, the R_{ct} value was significantly decreased from 1679 to 483.4 Ω as increasing the BLs from 2 to 8 BLs. In contrast, Pd$_n$ electrodes indicated a considerably higher R_{ct} value of 1469 Ω even at 8 BLs, resulting in a low electrocatalytic activity of Pd$_n$ film electrodes. As shown in Figure S5d, for both the Au$_n$ and Pd$_n$ monometallic electrodes, the current density for HMF oxidation gradually increased with the increasing thickness, up to 14 BLs. However, the electrocatalytic performance began to decrease after a critical thickness was reached, due to the limitation of the mass transfer of HMF into the 3D electrodes. In order to identify the origin of the limited mass transfer after a critical thickness, the average BL thickness of Pd$_n$ films was determined by a surface profilometer (Figure S7). Interestingly, it was found that the average BL thickness of Pd$_n$ films

above 12 BLs (24.1 nm/BL) was considerably higher than that of early deposition stage (11.3 nm/BL). As similarly observed in other LbL-assembled films, the increased BL thickness could result from the increased roughness and interdiffusion of polyions within the LbL films.[32,33] Thus, the mass transfer was more critically limited at a higher number of BLs.

The current density of the Au$_n$ electrodes was higher than that of the Pd$_n$ electrodes (Figure S5c), whereas the Pd$_n$ electrodes exhibited a significantly lower peak potential (0.77 V vs RHE) than the Au$_n$ electrodes (1.2 V vs RHE). For these reasons, we expected that the bimetallic system combining Au and Pd NPs would improve the electrocatalytic performance, reducing the onset potential as well as increasing the anodic current for HMF oxidation.

On the basis of the optimized catalytic activity of the monometallic system at 14 BLs achieved through a fine balance between the HMF oxidation and diffusion process, four different bimetallic systems with 7 BLs of each metal NP (a total of 14 BLs, i.e., the optimal number) were fabricated with Au and Pd NPs: Au$_7$/Pd$_7$, Pd$_7$/Au$_7$, (AuPd)$_7$, and (PdAu)$_7$. All the assembled electrodes were investigated to identify the architecture−performance relationship toward HMF oxidation. As indicated by the LSV measurements (Figure 2), all bimetallic film electrodes exhibited significantly improved electrocatalytic activity, with an increased peak
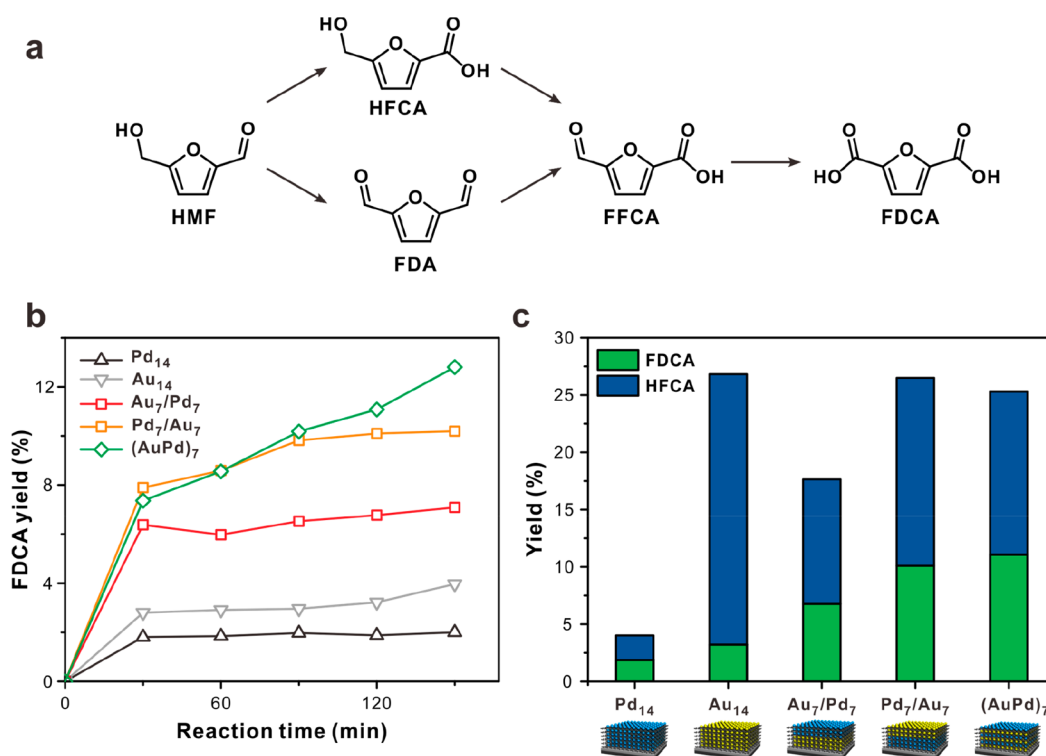
Figure 4. (a) Schematic reaction pathways for the sequential oxidation of HMF to FDCA through various reaction intermediates. (b) Yield of the final product FDCA from each electrode during the electrochemical oxidation and (c) comparison of the relative concentration ratio between 5-hydroxymethyl-2-furancarboxylic acid (HFCA) and FDCA for different types of electrodes at 120 min. Reaction conditions: 10 mL of 5.0 mM HMF in 1.0 M KOH; anode potential of 0.82 V *vs* RHE.

current density and a low peak potential, in comparison with the monometallic Au$_{14}$ and Pd$_{14}$ electrodes. Among them, the fully alternating (Pd/Au)$_7$ bimetallic electrode exhibited the highest current density of 3.24 mA cm^{-2}, which was a 225% improvement in comparison with that of the monometallic Pd$_{14}$ electrode. The Pd$_7$/Au$_7$ bimetallic electrode had the lowest peak potential (0.76 V *vs* RHE), clearly suggesting that there was a synergistic effect for HMF oxidation within the heterogeneous bimetallic 3D multilayer electrodes. Since the difference between fully alternating bimetallic (AuPd)$_7$ electrode and (PdAu)$_7$ electrode was insignificant, (AuPd)$_7$ was chosen as the representative electrode to investigate further in this study.

For successful coupling of the full cell system with simultaneous FDCA and H$_2$ production, the LbL-assembled multilayer electrodes require high HER performance in the presence of HMF. Here, the electrocatalytic activity for the HER was investigated for the synthesized multilayer electrodes in the absence and presence of 10 mM HMF (Figure S8). Interestingly, there was no significant change in the LSV curve, indicating that the cathodic H$_2$ evolution was not influenced by the presence of HMF. In addition, this result suggests that hydrogen is originated from water instead of HMF. According to the previous literature, the origin of H$_2$ in electrochemical reforming was suggested to be water as revealed by the deuterated solvent experiments.[34]

The electrocatalytic activity for the HER in the HMF solution was then investigated for LbL-assembled multilayer electrodes (Figure 3). When the Au and Pd NPs were assembled together, the HER activity was significantly improved, with a lower onset potential and a higher current density, compared with the case of the monometallic

electrodes. Among the electrodes, the fully alternating (AuPd)$_7$ electrode exhibited the best performance, with the highest current density (−8.62 mA cm^{-2}) at −0.4 V (*vs* RHE) and the lowest onset potential (−0.10 V *vs* RHE) at −0.2 mA cm^{-2}. The Au$_7$/Pd$_7$ electrode required a significantly higher overpotential of 0.18 V (*vs* RHE) and had a lower current density (5.55 mA cm^{-2}), whereas the Pd$_7$/Au$_7$ electrode exhibited similar HER catalytic performance to (AuPd)$_7$, which was similar to the tendency of the electrocatalytic performance for HMF oxidation. Furthermore, to identify HER performance with respect to the number of BLs, the electrocatalytic activity was compared with (AuPd)$_n$ film electrodes (n = 4−7). While the HER activity was improved with respect to the number of BLs (Figure S9), the number of BLs was fixed to 7 BLs for each NP throughout this study, as it is optimized for the anodic reaction.

Mechanistic Study and Architecture−Performance Relationships. Encouraged by the improved electrocatalytic behavior of the bimetallic Au and Pd NPs toward electrocatalytic activity, we then examined the relationship between the architecture of the multilayer electrodes and the electrochemical behavior in further detail. At first, the catalytic mechanism of HMF oxidation was investigated. Generally, there are two possible pathways in the HMF oxidation reaction to produce FDCA through various reaction intermediates of different oxidation levels (Figure 4a).[17,35,36] To investigate the mechanisms of HMF oxidation for the Au-Pd bimetallic system, chronoamperometric (CA) tests were performed at a constant potential of 0.82 V (*vs* RHE), which corresponds to the peak potential of HMF oxidation. During the electrocatalytic oxidation, the concentration of HMF and its corresponding oxidation products with various LbL-assembled

Scheme 2. (a) Schematic Reaction Pathways for the Sequential Oxidation of HMF with Pd and Au NPs and Putative Reaction Mechanism with (b) Pd_7/Au_7 and (c) Au_7/Pd_7 Multilayer Electrodes for Converting HMF into FDCA
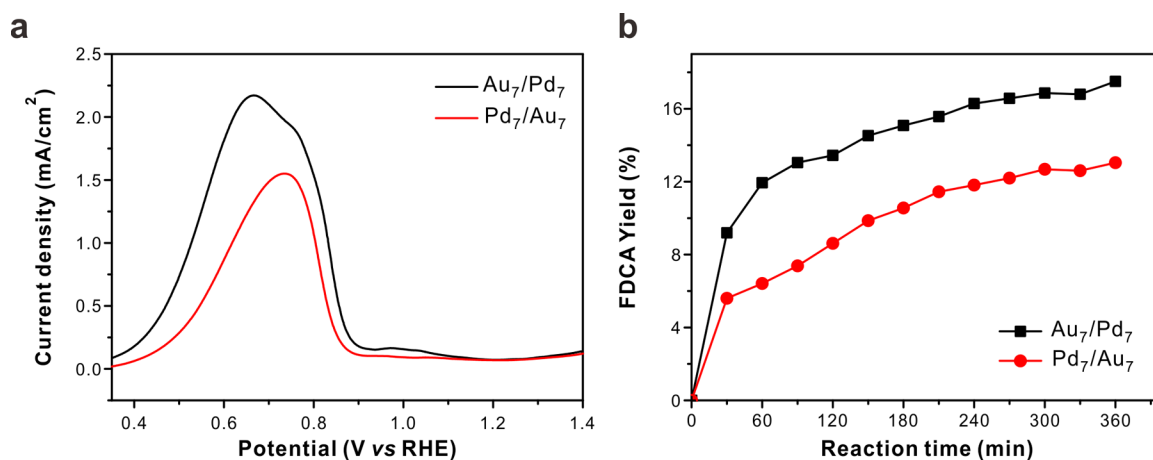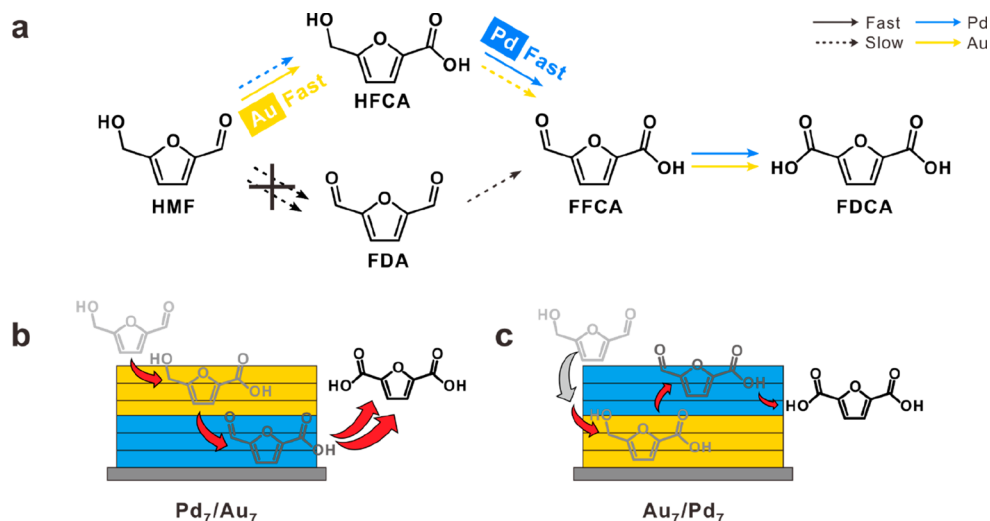

Figure 5. (a) LSV curves with Au_7/Pd_7 and Pd_7/Au_7 multilayer electrodes for converting HFCA into FDCA. (b) FDCA yield from HFCA measured *via* HPLC. All LSVs were recorded in 1.0 M KOH with 10 mM HFCA, at a scan rate of 2.0 mV s^{-1}.

electrodes were monitored by high-performance liquid chromatography (HPLC) (Figure 4b,c and Figure S10). Among them, HFCA appeared as a major intermediate, whereas 2,5-furandicarbaldehyde (FDA) was not observed in the overall reaction (Figure S10b). This observation indicates that the oxidation of the aldehyde group was more favorable than that of the alcohol group of HMF in our system.

For both the mono- and bimetallic electrodes, the conversion of HMF occurred rapidly in the early stage (within 30 min), except only for the monometallic Pd_{14} electrode, which exhibited a significantly low HMF conversion of 4.92% after 30 min (Figure S11). It is also of note that the monometallic Au_{14} electrode displayed a poor yield of the final product FDCA (3.22%) (Table S2), albeit with a high yield of HFCA (23.6%) from HMF (Figure 4c), indicating that the Au NPs were more effective than Pd NPs for the oxidation of HMF to HFCA. In contrast, while the HMF conversion by the Pd NPs was significantly slower, it resulted in high selectivity for FDCA. In other words, the conversion efficiency from HFCA to FDCA for Pd_{14} was 53.2%, which was much higher than that of Au_{14} (12.0%), in addition to the significantly reduced HFCA yield for all the Pd-supported Au bimetallic

electrodes. These results indicate that the conversion of HFCA was more favorable for the Pd NPs than for the Au NPs.

After the slow rate-limiting steps for pure Au and Pd monometallic electrodes were identified, conclusions could be drawn regarding the benefit of Au–Pd bimetallic electrodes for FDCA production. Combining both Au and Pd NPs led to more facile aldehyde oxidation at a low potential with an enhanced alcohol oxidation activity in comparison to individual single components. Indeed, the bimetallic system exhibited an FDCA yield more than 2-fold higher than that of the monometallic electrodes. More interestingly, even with the identical composition of NPs, the electrocatalytic activity was tunable according to the location of the NPs within the multilayer electrodes, which could be related to the stepwise reaction pathway involved in the HMF oxidation. For instance, although the $(AuPd)_7$ and Pd_7/Au_7 electrodes exhibited similar FDCA yields, there was a significant difference in electrochemical activity, between the electrodes with opposite layering sequences, that is, Au_7/Pd_7 (Pd layer atop Au layer) and Pd_7/Au_7 (Au layer atop Pd layer) (Figure 4b,c). The current density of the Pd_7/Au_7 electrode (3.09 mA cm^{-2}) was significantly higher than that of the Au_7/Pd_7 electrode (2.53 mA cm^{-2}). Furthermore, the Pd_7/Au_7 electrode exhibited a

Scheme 3. HER Mechanisms for the (a) (AuPd)$_7$, (b) Pd$_7$/Au$_7$, and (c) Au$_7$/Pd$_7$ Multilayer Electrodes[a]
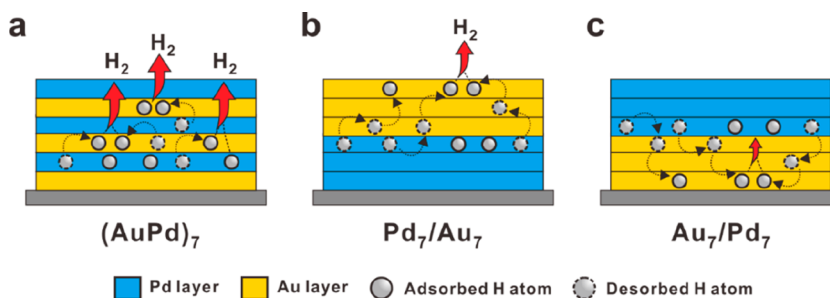
[a]Gray balls with solid and dashed lines represent adsorbed (H$_{ads}$) and desorbed H atoms, respectively.

higher yield of both FDCA (16.4%) and HFCA (10.1%) in comparison with the Au$_7$/Pd$_7$ electrode.

Because Au NPs favored the conversion of HMF into HFCA, HMF is rapidly oxidized to HFCA when Au NPs are located at the outer layer (Scheme 2a). Indeed, both the Au$_{14}$ and Pd$_7$/Au$_7$ electrodes exhibited a high concentration of HFCA (Figure 4c). Subsequently, the generated HFCA served as a reactant on Pd NPs to facilitate afford the conversion toward the final product, that is, FDCA. The Au NPs supplied an additional reactant, that is, HFCA, to the surface of the Pd NPs and increased the concentration, resulting in enhanced mass transfer for the 3D multilayer electrodes. Therefore, when Au NPs were located at the outer layer, as in the case of the Pd$_7$/Au$_7$ electrode, the current density was high owing to the enhanced mass transfer into inner-layer Pd NPs for the effective oxidation toward FDCA.

To verify this interpretation, we investigated the electrocatalytic oxidation of the intermediate HFCA compound using Pd$_7$/Au$_7$ and Au$_7$/Pd$_7$ electrodes (Figure 5). In contrast to the case of HMF oxidation, the Au$_7$/Pd$_7$ electrode exhibited a higher FDCA yield (17.5%) and current density (2.17 mA cm^{-2}) than the Pd$_7$/Au$_7$ electrode (13.0% and 1.55 mA cm^{-2}, respectively). Thus, when Pd NPs existed at the outer layer (Au$_7$/Pd$_7$ electrode), the electrocatalytic performance for converting HFCA was high, because Pd NPs could rapidly oxidize HFCA to FDCA. These differences in the electrocatalytic performance and product distribution clearly demonstrate that the reaction pathway of HMF oxidation is highly dependent on the types of catalysts and the architecture of bimetallic electrodes, which is difficult to observe in other conventional electrode manufacturing techniques.

In addition, Faradaic efficiency for anode is calculated with each multilayer film electrode (Table S3). Interestingly, monometallic Pd$_{14}$ film and all bimetallic films showed a good faradaic efficiency for producing FDCA (72.8–85.8%), whereas Au$_{14}$ has a poor efficiency of 45.8% albeit with the high charge passed. This result further supports the proposed mechanism that Au NP favors to convert HMF to HFCA, while it is still undesirable to yield the final product, FDCA (Scheme 2).

To further correlate the nanoarchitecture and performance of the multilayer electrodes with the mechanisms for the HER, the electrochemical kinetics for the HER was investigated using the Tafel slopes of the LbL-assembled electrodes. As described in the section related to the HMF oxidation reaction, the HER activity strongly depends on the architecture of the multilayer electrodes. For example, both monometallic electrodes—Au$_{14}$ and Pd$_{14}$—exhibited a low HER activity, with a high Tafel slope of 288 and 174 mV dec^{-1}, respectively, in the

Tafel region from −0.06 to −0.33 V (Figure S12). In contrast, the bimetallic (AuPd)$_7$ and Pd$_7$/Au$_7$ electrodes exhibited significantly improved kinetics, with a lower Tafel slope of 105−109 mV dec^{-1}, which is comparable to the values reported for other catalysts.[37,38]

It is widely known that in the first step of the HER, a water molecule receives an electron and generates an adsorbed H atom (H$_{ads}$) as an intermediate (Volmer reaction) on the surface of the catalysts.[39,40] In the second step, the electron is transferred to the H$_{ads}$, and generated H$_2$ molecules are then released on the catalyst surface *via* a Tafel or Heyrovsky reaction. Therefore, the optimal Gibbs free energy for H$_{ad}$ between the adsorption and desorption of hydrogen in the volcano plots ($\Delta G_{H_{ad}} \approx 0$) is necessary to develop highly efficient HER electrocatalysts.

According to the volcano plots for the HER, which are correlated to the binding energy of H$_{ads}$, Pd has a small energy barrier with negative $\Delta G_{H_{ad}}$ for the adsorption of protons.[40−44] On the other hand, Au, which has a high $\Delta G_{H_{ad}}$ for H$_{ad}$ ($\Delta G_{H_{ad}} > 0$), can participate more easily in the desorption process. Therefore, the diffusion coefficient of H$_{ads}$ atoms on Au is approximately 1.47×10^{-3} cm^2 s^{-1},[45] which is significantly higher than that on a Pd surface (1.30×10^{-7} cm^2 s^{-1}).[46] According to these distinctive features of relatively adsorption-like Pd and desorption-like Au, H$_{ads}$ was more favorable to form on the surface of Pd layers in our Au-Pd bimetallic multilayer electrodes. The hydrogen coverage on the restricted Pd surface increases rapidly, and the excessive H$_{ads}$ atoms begin to spill over from hydrogen-rich Pd to the nearby hydrogen-poor Au NP layers, freeing Pd sites that can be filled by newly H$_{ads}$. Thus, in addition to the possible desorption of hydrogen on the Pd surface, the chemical desorption of spilled over hydrogen can occur on the adjacent Pd-Au and/or Au-Au layers within the multilayer electrodes. Consequently, the electrocatalytic HER activity of the bimetallic electrodes is significantly improved in comparison with that of the monometallic electrodes, because the excessive H$_{ads}$ produced on the Pd layers quickly spills over to the neighboring Au and then undergoes fast desorption (Scheme 3). According to the previous researches, the effect of hydrogen spillover in heterogeneous catalysts has been reported for diverse alloy systems.[44,45,47−50] In concert with our results, by employing both experimental and theoretical approaches, Sykes *et al.* demonstrated a similar spillover phenomenon of hydrogen onto Au-supported Pd clusters.[50]

For these reasons, a large number of contact layers between Au and Pd NPs in the fully alternating (AuPd)$_7$ multilayer electrode yielded a low R_{ct} of 135 Ω (Figure S13), which
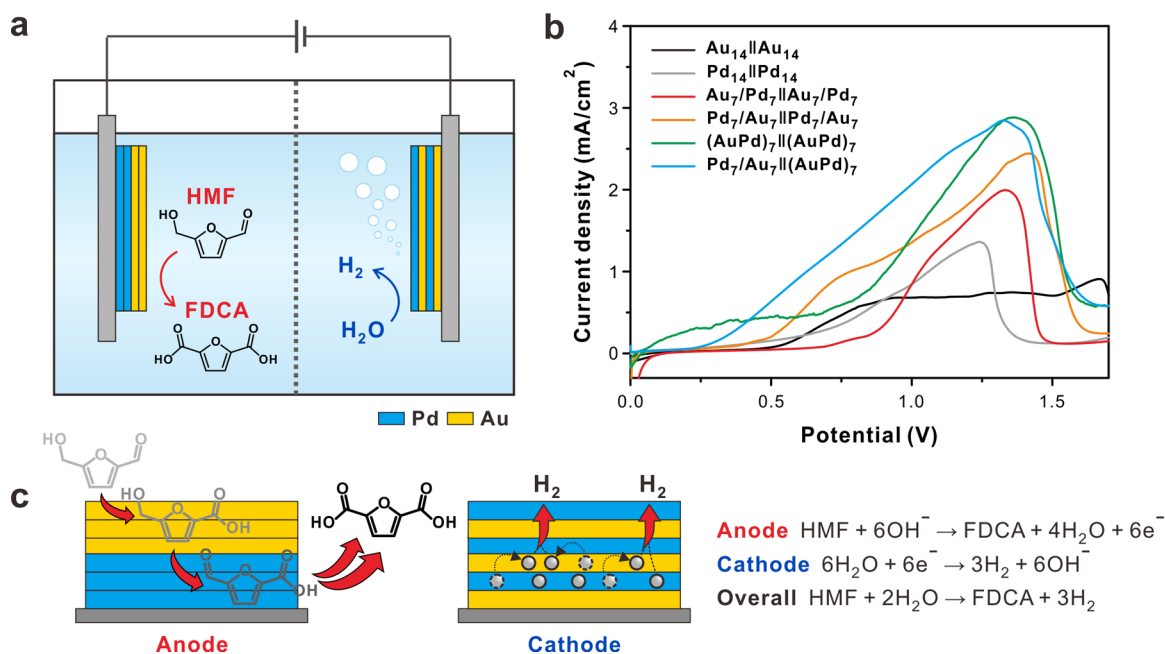
Figure 6. (a) Illustration of the two-electrode full-cell system of $Pd_7/Au_7\|(AuPd)_7$ used in this study for the simultaneous generation of FDCA in the anode and H_2 in the cathode. (b) LSV curves of the two-electrode full-cell system for HMF oxidation in a 1.0 M KOH solution with 10 mM HMF, collected using a scan rate of 2.0 mV s^{-1}. (c) Schematic of the Pd_7/Au_7 multilayer anode and the $(AuPd)_7$ multilayer cathode with the corresponding electrocatalytic reactions. Gray balls with solid and dashed lines represent adsorbed (H_{ads}) and desorbed H atoms, respectively. Note that the carboxylic acid groups of FDCA and intermediates are deprotonated in the 1.0 M KOH solution.

eventually resulted in better performance in comparison with the other bimetallic electrodes, that is, Pd_7/Au_7 and Au_7/Pd_7. In the case of the same number of contact layers between Au and Pd layers, for example, Au_7/Pd_7 and Pd_7/Au_7, Pd NPs located at the inner layer (Pd_7/Au_7) may be more beneficial not only for forming a high concentration profile of H_{ads} within the Nernst diffusion layer at the bottom end of the catalytic electrodes underneath but also for releasing H_{ads} on the Au surface of the outer layer near electrolytes for the desorption process *via* Heyrovsky reaction. As a result, the HER kinetics could be facilitated with a low R_{ct} value of 190 Ω compared to a high R_{ct} value of 1397 Ω for the Au_7/Pd_7 electrode.

Full-Cell Performance. According to our investigation of the nanoarchitecture-related electrocatalytic performance, we fabricated the full-cell system exclusively with LbL-assembled electrodes. The system was optimized for the respective half-cell reactions. Because the full-cell system requires a higher energy than the half-cell system, the overall catalytic perform-ance differed considerably depending on the architecture of the multilayer film electrodes. When the two-electrode system was coupled with the same multilayer electrodes in both anode and cathode, $(AuPd)_7\|(AuPd)_7$ demonstrated the highest current density among all combinations because the fully alternating $(AuPd)_7$ electrode showed a good activity for both HMF oxidation and HER (Figure 6 and Figure S14). Furthermore, when we combined the Pd_7/Au_7 film as the anode and $(AuPd)_7$ as the cathode, the full-cell electrocatalytic perform-ance was more improved compared to that of $Pd_7/Au_7\|Pd_7/Au_7$ system, owing to the outstanding performance of $(AuPd)_7$ film toward HER.

These results confirmed that a rational strategy for controlling the architecture is essential for controlling the electrocatalytic activity. This fine control is particularly important in the case of cascade or tandem reactions, because the deposition sequence of active NPs is critical, as each type

of NP has different kinetics and a different energy barrier for the electrochemical reactions. As demonstrated in this study, HMF oxidation requires several oxidative processes to produce FDCA. While Au NPs are more favorable for converting HMF into the intermediate HFCA, Pd NPs can rapidly convert HFCA into the final product FDCA. In the case of the HER, an architecture with adjacent Pd and Au (fully alternating $(AuPd)_7$ electrode) is highly desirable for the rapid spillover of adsorbed hydrogen from the Pd NPs to the Au NPs.

CONCLUSION

In summary, we systematically examined LbL-assembled bimetallic electrodes to reveal the architecture−performance relationship for electrochemical HMF oxidation and H_2 production. The electrocatalytic activity with LbL-assembled multilayer electrode is mainly governed by the thickness and the architecture of the electrodes. Even with the identical composition of NPs, when Au NPs were located at the outer layer, as in the case of Pd_7/Au_7 electrode, the yield of FDCA was higher compared with that for Au_7/Pd_7, due to the enhanced mass transfer of HFCA into inner-layer Pd NPs. In the case of the HER, an architecture with adjacent Pd and Au (fully alternating $(AuPd)_7$ electrode) was highly desirable for the rapid spillover of hydrogen from the Pd NPs to the Au NPs. Furthermore, a full-cell electrochemical system with the optimized electrodes for HMF oxidation and the HER was successfully controlled according to the assembled combina-tions of electrodes. We believe our systematic study involving LbL-assembled electrodes can be extended to the rational design of other highly active and selective catalysts for various oxidation reactions in ecofriendly processes.

METHODS

Preparation of Nanosized Graphene Oxide (nGO). nGO was synthesized from graphite nanofibers (Catalytic Materials, United

States) according to a previously reported method.[51] Graphite oxide was synthesized by the modified Hummers method and exfoliated to obtain a brown dispersion of nGO under ultrasonication at a concentration of 0.50 mg/mL.

Preparation of Au and Pd NPs. The DMAP-stabilized Au and Pd NPs were prepared *via* spontaneous phase transfer from an organic solvent, using a previously reported method.[52]

LbL Assembly of Hybrid Electrode Films. An ITO-coated glass substrate was cleaned *via* sonication in deionized (DI) water, acetone, and ethanol for 10 min. Si and quartz substrates were cleaned with a piranha solution to remove organic contamination, followed by treatment with (3-aminopropyl)triethoxysilane to introduce a positively charged hydrophilic surface. These substrates were first dipped into a negatively charged nGO solution (0.50 mg/mL) with a pH of 4 for 10 min. They were then dipped into DI water for 1 min three times to remove loosely bound nGO. Subsequently, the substrates were dipped into a positively charged DMAP-coated Au or Pd NP suspension with a pH of 11 for 10 min and washed with DI water three times for 1 min, yielding a 1-BL film of Au_1 or Pd_1, respectively. The foregoing procedures were repeated to obtain the desired number of BLs (n). Multicomponent assembly was conducted using the identical procedure with both Au and Pd NP suspensions. All the as-assembled multilayer films were subjected to thermal reduction at 150 °C for 12 h in an oven before the electrochemical analysis.

Electrochemical Analysis. Electrochemical experiments were performed using a standard three-electrode cell configuration (Bio-Logic Science Instruments, VSP). A Pt wire was used as a counter electrode, and Hg/HgO was used as a reference electrode. The working electrode was a multilayer thin film assembled on ITO-coated glass. LSV and cyclic voltammetry were performed between −0.6 and 0.6 V *vs* Hg/HgO in a 1.0 M KOH solution with a 10 mM HMF solution at 25 °C at a scan rate of 20 mV s^{-1}. The current density was calculated by dividing with the geometric area (cm^2) of the as-prepared LbL-assembled electrodes. The values of the potential were converted from *vs* Hg/HgO to *vs* RHE as follows: Hg/HgO + 0.924 V = RHE. Electrochemical impedance spectroscopy measurements were performed in the frequency range of 100 kHz to 100 mHz under alternating current.

Characterizations. The absorbance of the thin films was characterized by using UV−vis spectroscopy (UV-2550, Shimadzu). The thickness of the as-prepared samples on Si substrates was measured using a surface profiler (DektakXT Stylus Profiler, Bruker). The surface morphology of the samples was investigated using atomic force microscopy (AFM, NX-10, Park Systems) in a noncontact mode. The size and morphology of the prepared NPs were measured by transmission electron microscopy (TEM, JEM-2100, JEOL). The cross-sectional TEM samples were prepared using a focused ion-beam (FIB) technique (Crossbeam 540, ZEISS), and cross-sectional images were obtained by high-resolution transmission electron microscopy (HR-TEM), high-angle annular dark-field scanning transmission electron microscopy (HAADF-STEM), and energy dispersive X-ray spectroscopy (EDS, JEM-F200, JEOL). The active mass of each material adsorbed onto the film surface was analyzed by a quartz crystal microbalance (QCM, QCM200, Stanford Research Systems).[28] The intermediates during the reaction were investigated by high-performance liquid chromatography (HPLC, Shimadzu Prominence). To study the oxidation products of HMF, 0.2 mL of electrolyte was collected every 30 min during chronoamperometry at 0.82 V (*vs* RHE) and then analyzed by HPLC at room temperature. The products, including HMF, HFCA, FFCA, and FDCA, were separated using a C18 column (200 × 4.6 mm^2). The furan compounds were detected using a UV detector at 265 nm. The mobile phase was composed of water and methanol, with a ratio of 90:10, and the flow rate was set as 1.0 mL/min. Each concentration of products was quantified by a calibration curve with standard samples.

ASSOCIATED CONTENT

ⓈI Supporting Information

The Supporting Information is available free of charge at https://pubs.acs.org/doi/10.1021/acsnano.0c00581.

Detailed characterizations, TEM, UV−vis spectra, AFM images, electrochemical measurements, and HPLC analysis with additional tables (PDF)

AUTHOR INFORMATION

Corresponding Author

Byeong-Su Kim − *Department of Chemistry, Yonsei University, Seoul 03722, Republic of Korea;* ⓘ orcid.org/0000-0002-6419-3054; Email: bskim19@yonsei.ac.kr

Authors

Minju Park − *Department of Chemistry, Yonsei University, Seoul 03722, Republic of Korea; Department of Chemical Engineering, Ulsan National Institute of Science and Technology (UNIST), Ulsan 44919, Republic of Korea;* ⓘ orcid.org/0000-0002-5508-6652

Minsu Gu − *Department of Chemistry, Yonsei University, Seoul 03722, Republic of Korea; Department of Chemistry, The University of Texas at Austin, Austin, Texas 78712, United States;* ⓘ orcid.org/0000-0002-6270-7496

Complete contact information is available at:
https://pubs.acs.org/10.1021/acsnano.0c00581

Author Contributions

‖These authors contributed equally to this work.

Notes

The authors declare no competing financial interest.

REFERENCES

(1) Werpy, T.; Petersen, G. *Top Value Added Chemicals from Biomass Vol. I-Results of Screening for Potential Candidates from Sugars and Synthesis Gas*, NREL/TP-510-35523; National Renewable Energy Laboratory: Golden, CO, 2004.

(2) Goldemberg, J. Ethanol for a Sustainable Energy Future. *Science* **2007**, *315*, 808−810.

(3) Ermakova, M. A.; Ermakov, D. Y.; Kuvshinov, G. G. Effective Catalysts for Direct Cracking of Methane to Produce Hydrogen and Filamentous Carbon: Part I. Nickel Catalysts. *Appl. Catal., A* **2000**, *201*, 61−70.

(4) Jin, H.; Wang, J.; Su, D.; Wei, Z.; Pang, Z.; Wang, Y. *In Situ* Cobalt−Cobalt Oxide/N-Doped Carbon Hybrids as Superior Bifunctional Electrocatalysts for Hydrogen and Oxygen Evolution. *J. Am. Chem. Soc.* **2015**, *137*, 2688−2694.

(5) Jiang, N.; You, B.; Sheng, M.; Sun, Y. Electrodeposited Cobalt-Phosphorous-Derived Films as Competent Bifunctional Catalysts for Overall Water Splitting. *Angew. Chem., Int. Ed.* **2015**, *54*, 6251−6254.

(6) Luo, J.; Im, J.-H.; Mayer, M. T.; Schreier, M.; Nazeeruddin, M. K.; Park, N.-G.; Tilley, S. D.; Fan, H. J.; Grätzel, M. Water Photolysis at 12.3% Efficiency *via* Perovskite Photovoltaics and Earth-Abundant Catalysts. *Science* **2014**, *345*, 1593−1596.

(7) Zeng, K.; Zhang, D. Recent Progress in Alkaline Water Electrolysis for Hydrogen Production and Applications. *Prog. Energy Combust. Sci.* **2010**, *36*, 307−326.

(8) Liu, J.; Liu, Y.; Liu, N.; Han, Y.; Zhang, X.; Huang, H.; Lifshitz, Y.; Lee, S.-T.; Zhong, J.; Kang, Z. Metal-Free Efficient Photocatalyst for Stable Visible Water Splitting *via* a Two-Electron Pathway. *Science* **2015**, *347*, 970−974.

(9) Take, T.; Tsurutani, K.; Umeda, M. Hydrogen Production by Methanol−Water Solution Electrolysis. *J. Power Sources* **2007**, *164*, 9−16.

(10) Chen, Y. X.; Lavacchi, A.; Miller, H. A.; Bevilacqua, M.; Filippi, J.; Innocenti, M.; Marchionni, A.; Oberhauser, W.; Wang, L.; Vizza, F. Nanotechnology Makes Biomass Electrolysis More Energy Efficient Than Water Electrolysis. *Nat. Commun.* **2014**, *5*, 4036.

(11) Zhao, X.; Dai, L.; Qin, Q.; Pei, F.; Hu, C.; Zheng, N. Self-Supported 3D PdCu Alloy Nanosheets as a Bifunctional Catalyst for Electrochemical Reforming of Ethanol. *Small* **2017**, *13*, 1602970.

(12) Schalenbach, M.; Carmo, M.; Fritz, D. L.; Mergel, J.; Stolten, D. Pressurized PEM Water Electrolysis: Efficiency and Gas Crossover. *Int. J. Hydrogen Energy* **2013**, *38*, 14921−14933.

(13) Yu, Z.-Y.; Lang, C.-C.; Gao, M.-R.; Chen, Y.; Fu, Q.-Q.; Duan, Y.; Yu, S.-H. Ni−Mo−O Nanorod-Derived Composite Catalysts for Efficient Alkaline Water-to-Hydrogen Conversion *via* Urea Electrolysis. *Energy Environ. Sci.* **2018**, *11*, 1890−1897.

(14) van Putten, R.-J.; van der Waal, J. C.; de Jong, E.; Rasrendra, C. B.; Heeres, H. J.; de Vries, J. G. Hydroxymethylfurfural, a Versatile Platform Chemical Made from Renewable Resources. *Chem. Rev.* **2013**, *113*, 1499−1597.

(15) Bozell, J. J.; Petersen, G. R. Technology Development for the Production of Biobased Products from Biorefinery Carbohydrates—The US Department of Energy's "Top 10" Revisited. *Green Chem.* **2010**, *12*, 539−554.

(16) Saha, B.; Dutta, S.; Abu-Omar, M. M. Aerobic Oxidation of 5-Hydroxylmethylfurfural with Homogeneous and Nanoparticulate Catalysts. *Catal. Sci. Technol.* **2012**, *2*, 79−81.

(17) Siyo, B.; Schneider, M.; Radnik, J.; Pohl, M.-M.; Langer, P.; Steinfeldt, N. Influence of Support on the Aerobic Oxidation of HMF into FDCA over Preformed Pd Nanoparticle Based Materials. *Appl. Catal., A* **2014**, *478*, 107−116.

(18) Davis, S. E.; Houk, L. R.; Tamargo, E. C.; Datye, A. K.; Davis, R. J. Oxidation of 5-Hydroxymethylfurfural over Supported Pt, Pd and Au Catalysts. *Catal. Today* **2011**, *160*, 55−60.

(19) Mishra, D. K.; Lee, H. J.; Kim, J.; Lee, H.-S.; Cho, J. K.; Suh, Y.-W.; Yi, Y.; Kim, Y. J. MnCo₂O₄ Spinel Supported Ruthenium Catalyst for Air-Oxidation of HMF to FDCA under Aqueous Phase and Base-Free Conditions. *Green Chem.* **2017**, *19*, 1619−1623.

(20) Kwon, Y.; Schouten, K. J. P.; van der Waal, J. C.; de Jong, E.; Koper, M. T. M. Electrocatalytic Conversion of Furanic Compounds. *ACS Catal.* **2016**, *6*, 6704−6717.

(21) Kwon, Y.; Birdja, Y. Y.; Raoufmoghaddam, S.; Koper, M. T. M. Electrocatalytic Hydrogenation of 5-Hydroxymethylfurfural in Acidic Solution. *ChemSusChem* **2015**, *8*, 1745−1751.

(22) Chadderdon, D. J.; Xin, L.; Qi, J.; Qiu, Y.; Krishna, P.; More, K. L.; Li, W. Electrocatalytic Oxidation of 5-Hydroxymethylfurfural to 2,5-Furandicarboxylic Acid on Supported Au and Pd Bimetallic Nanoparticles. *Green Chem.* **2014**, *16*, 3778−3786.

(23) You, B.; Jiang, N.; Liu, X.; Sun, Y. Simultaneous H₂ Generation and Biomass Upgrading in Water by an Efficient Noble-Metal-Free Bifunctional Electrocatalyst. *Angew. Chem., Int. Ed.* **2016**, *55*, 9913−9917.

(24) You, B.; Liu, X.; Jiang, N.; Sun, Y. A General Strategy for Decoupled Hydrogen Production from Water Splitting by Integrating Oxidative Biomass Valorization. *J. Am. Chem. Soc.* **2016**, *138*, 13639−13646.

(25) Song, F.; Li, W.; Yang, J.; Han, G.; Liao, P.; Sun, Y. Interfacing Nickel Nitride and Nickel Boosts Both Electrocatalytic Hydrogen Evolution and Oxidation Reactions. *Nat. Commun.* **2018**, *9*, 4531.

(26) You, B.; Liu, X.; Liu, X.; Sun, Y. Efficient H₂ Evolution Coupled with Oxidative Refining of Alcohols *via* a Hierarchically Porous Nickel Bifunctional Electrocatalyst. *ACS Catal.* **2017**, *7*, 4564−4570.

(27) Gu, M.; Choi, J.; Lee, T.; Park, M.; Shin, I.-S.; Hong, J.; Lee, H.-W.; Kim, B.-S. Diffusion Controlled Multilayer Electrocatalysts *via* Graphene Oxide Nanosheets of Varying Sizes. *Nanoscale* **2018**, *10*, 16159−16168.

(28) Gu, M.; Kim, B.-S. Unraveling the Importance of Controlled Architecture in Bimetallic Multilayer Electrode toward Efficient Electrocatalyst. *Nano Energy* **2016**, *30*, 658−666.

(29) Lee, T.; Min, S. H.; Gu, M.; Jung, Y. K.; Lee, W.; Lee, J. U.; Seong, D. G.; Kim, B.-S. Layer-by-Layer Assembly for Graphene-Based Multilayer Nanocomposites: Synthesis and Applications. *Chem. Mater.* **2015**, *27*, 3785−3796.

(30) Ahn, E.; Lee, T.; Gu, M.; Park, M.; Min, S. H.; Kim, B.-S. Layer-by-Layer Assembly for Graphene-Based Multilayer Nanocomposites: The Field Manual. *Chem. Mater.* **2017**, *29*, 69−79.

(31) Ahn, E.; Gaiji, H.; Kim, T.; Abderrabba, M.; Lee, H.-W.; Kim, B.-S. Graphene Oxide Nanosheet as a Two-Dimensional Polyelectrolyte: pH-Responsive Behavior of a Multilayered Nanomembrane. *J. Membr. Sci.* **2019**, *585*, 191−198.

(32) Zacharia, N. S.; DeLongchamp, D. M.; Modestino, M.; Hammond, P. T. Controlling Diffusion and Exchange in Layer-by-Layer Assemblies. *Macromolecules* **2007**, *40*, 1598−1603.

(33) DeLongchamp, D. M.; Kastantin, M.; Hammond, P. T. High-Contrast Electrochromism from Layer-by-Layer Polymer Films. *Chem. Mater.* **2003**, *15*, 1575−1586.

(34) Wei, X.; Wang, S.; Hua, Z.; Chen, L.; Shi, J. Metal−Organic Framework Nanosheet Electrocatalysts for Efficient H₂ Production from Methanol Solution: Methanol-Assisted Water Splitting or Methanol Reforming? *ACS Appl. Mater. Interfaces* **2018**, *10*, 25422−25428.

(35) Ardemani, L.; Cibin, G.; Dent, A. J.; Isaacs, M. A.; Kyriakou, G.; Lee, A. F.; Parlett, C. M. A.; Parry, S. A.; Wilson, K. Solid Base Catalysed 5-HMF Oxidation to 2,5-FDCA over Au/Hydrotalcites: Fact or Fiction? *Chem. Sci.* **2015**, *6*, 4940−4945.

(36) McKenna, S. M.; Mines, P.; Law, P.; Kovacs-Schreiner, K.; Birmingham, W. R.; Turner, N. J.; Leimkühler, S.; Carnell, A. J. The Continuous Oxidation of HMF to FDCA and the Immobilisation and Stabilisation of Periplasmic Aldehyde Oxidase (PaoABC). *Green Chem.* **2017**, *19*, 4660−4665.

(37) Ahn, E.; Kim, B.-S. Multidimensional Thin Film Hybrid Electrodes with MoS₂ Multilayer for Electrocatalytic Hydrogen Evolution Reaction. *ACS Appl. Mater. Interfaces* **2017**, *9*, 8688−8695.

(38) Huang, D.; Lu, J.; Li, S.; Luo, Y.; Zhao, C.; Hu, B.; Wang, M.; Shen, Y. Fabrication of Cobalt Porphyrin. Electrochemically Reduced Graphene Oxide Hybrid Films for Electrocatalytic Hydrogen Evolution in Aqueous Solution. *Langmuir* **2014**, *30*, 6990−6998.

(39) Li, Y.; Wang, H.; Xie, L.; Liang, Y.; Hong, G.; Dai, H. MoS₂ Nanoparticles Grown on Graphene: An Advanced Catalyst for the Hydrogen Evolution Reaction. *J. Am. Chem. Soc.* **2011**, *133*, 7296−7299.

(40) Sheng, W.; Myint, M.; Chen, J. G.; Yan, Y. Correlating the Hydrogen Evolution Reaction Activity in Alkaline Electrolytes with the Hydrogen Binding Energy on Monometallic Surfaces. *Energy Environ. Sci.* **2013**, *6*, 1509−1512.

(41) Seh, Z. W.; Kibsgaard, J.; Dickens, C. F.; Chorkendorff, I.; Nørskov, J. K.; Jaramillo, T. F. Combining Theory and Experiment in Electrocatalysis: Insights into Materials Design. *Science* **2017**, *355*, No. eaad4998.

(42) Allara, D. L.; Baca, A.; Pryde, C. A. Distortions of Band Shapes in External Reflection Infrared Spectra of Thin Polymer Films on Metal Substrates. *Macromolecules* **1978**, *11*, 1215−1220.

(43) Łukaszewski, M.; Czerwiński, A. Selected Electrochemical Properties of Pd-Au Alloys: Hydrogen Absorption and Surface Oxidation. *J. Solid State Electrochem.* **2008**, *12*, 1589−1598.

(44) Al-Odail, F. A.; Anastasopoulos, A.; Hayden, B. E. The Hydrogen Evolution Reaction and Hydrogen Oxidation Reaction on

Thin Film PdAu Alloy Surfaces. *Phys. Chem. Chem. Phys.* **2010**, *12*, 11398−11406.

(45) Guo, R.; Xu, X.; Xia, Y.; Huang, W.; Li, Z.; Teng, B. Insights into Electrocatalytic Hydrogen Evolution Reaction in Acidic Medium at *In-Situ* Dispersed Pt Atoms on Nanoporous Gold Films. *J. Catal.* **2018**, *368*, 379−388.

(46) Devanathan, M. A. V.; Stachurski, Z. The Adsorption and Diffusion of Electrolytic Hydrogen in Palladium. *Proc. R. Soc. London, Ser. A* **1962**, *270*, 90−102.

(47) Cornejo-Romero, J.; Solis-Garcia, A.; Vega-Diaz, S. M.; Fierro-Gonzalez, J. C. Reverse Hydrogen Spillover during Ethanol Dehydrogenation on TiO_2-Supported Gold Catalysts. *Mol. Catal.* **2017**, *433*, 391−402.

(48) Conner, W. C.; Falconer, J. L. Spillover in Heterogeneous Catalysis. *Chem. Rev.* **1995**, *95*, 759−788.

(49) Vayssilov, G. N.; Rösch, N. Reverse Hydrogen Spillover in Supported Subnanosize Clusters of the Metals of Groups 8 to 11. A Computational Model Study. *Phys. Chem. Chem. Phys.* **2005**, *7*, 4019−4026.

(50) Lucci, F. R.; Darby, M. T.; Mattera, M. F. G.; Ivimey, C. J.; Therrien, A. J.; Michaelides, A.; Stamatakis, M.; Sykes, E. C. H. Controlling Hydrogen Activation, Spillover, and Desorption with Pd-Au Single-Atom Alloys. *J. Phys. Chem. Lett.* **2016**, *7*, 480−485.

(51) Luo, J.; Cote, L. J.; Tung, V. C.; Tan, A. T. L.; Goins, P. E.; Wu, J.; Huang, J. Graphene Oxide Nanocolloids. *J. Am. Chem. Soc.* **2010**, *132*, 17667−17669.

(52) Gittins, D. I.; Caruso, F. Spontaneous Phase Transfer of Nanoparticulate Metals from Organic to Aqueous Media. *Angew. Chem., Int. Ed.* **2001**, *40*, 3001−3004.

NOTE ADDED AFTER ASAP PUBLICATION

This article published June 8, 2020 with an error in Figure 6. The figure was corrected and the article reposted June 10, 2020.